43rd AIAA Thermophysics Conference
25 - 28 June 2012, New Orleans, Louisiana

AIAA 2012-2751

Thermal Radiative Analysis of the HIFiRE-2 Scramjet Engine

Andrew J. Crow* and Iain D. Boyd†
University of Michigan, Ann Arbor, MI, 48109, USA
Michael S. Brown‡
Air Force Research Laboratory, WPAFB, OH, 45433, USA
Jiwen Liu§
Taitech, Inc, WPAFB, OH, 45433, USA

Thermal radiation is a poorly understood process in scramjet engines but may play a significant role in the flow and wall heating of the combustion chamber. Previous work has looked at the HyShot II combustion chamber and found the thermal radiation to be insignificant. The current work considers a combustion chamber similar to the HIFiRE-2 supersonic combustion chamber. The combustion flow is computed using a turbulent RANS fluid code, finding the convective heat flux to be on the order of 1.0 to 3.0 MW/m^2. The flow-field results are post-processed with a Discrete Ordinates Method radiative heat transfer code using a spectrally resolved narrow-band approximation resulting in a radiative heat flux to the wall of 15 to 56 kW/m^2. A method of estimating the epistemic uncertainty of the radiative wall heat flux stemming from the uncertainty in the spectral model found the radiative wall heat flux to vary by 11 to 15 %. The cooling of the flow due to radiation is predicted using an uncoupled method. Depending on the individual flow-path, the predicted temperature reduction due to radiation can range from 2 to 245 K. Thermal radiative measurements are obtained in an experimental setup of the HIFiRE-2 engine on the HIFiRE Direct-Connect Rig (HDCR) in theArc-Heated Scramjet Test Facility (AHSTF) at NASA Langley Research Center. An array of photodetectors gathered emission in the infrared along several lines-of-sight across the combustor exit. Predictions of radiation along these same lines are compared to the measurements indicating strengths and weaknesses of the simulation approach.

Nomenclature

a	Cell Face Area Vector, m^2
B_ν	Blackbody Intensity, W/(m^2 Hz Sr)
E	Estimated Error
F	Spectrally Integrated Heat Flux, W/m^2
F_ν	Spectrally Specific Heat Flux, W/(m^2 Hz)
f_ν	Scattering Redistribution Function
g	Correlated-k Quadrature Weight
I	Radiative Intensity Vector, W/(m^2 Sr)
I_ν	Radiative Intensity, W/(m^2 Hz Sr)
i	Location Index
j	Ordinate Index
k	Frequency Index

*Graduate Student, Student Member AIAA, email: ajcrow@umich.edu
†Professor, Fellow AIAA, email: iainboyd@umich.edu
‡Physicist, Associate Fellow AIAA, Aerospace Propulsion Division, email: Michael.Brown@wpafb.af.mil
§Senior Research Scientist, Associate Fellow AIAA, Aerospace Propulsion Division, email: Jiwen.Liu.ctr@wpafb.af.mil

l Correlated-k Quadrature Index
m Cell Face Index
N Maximum Index Number
n Species Index
Q Radiative Heat Loss Per Unit Volume, W/m^3
S_ν Spectral Line Strength, 1/m
s Trace Location, m
T Temperature, K
U System Uncertainty
V Cell Volume, m^3
X Mole Fraction
x Stream-wise Position, m
y Vertical Position, m
z Span-wise Position, m

Greek

θ Azimuthal Angle, rad
θ' Secondary Azimuthal Angle, rad
κ Extinction Coefficient, 1/m
μ Ordinate Angle Factor Relative to Path, $(\cos(\phi))$
μ' Secondary Ordinate Angle Factor Relative to Path, $(\cos(\phi'))$
ν Frequency, Hz
ρ Density, kg/m^3
ρ_n Normalized Number Density
σ Standard Deviation of Extinction Coefficient, 1/m
ϕ Vertical Angle, rad
ϕ' Secondary Vertical Angle, rad

Subscript

0 Nominal State
abs Frequency Specific Absorption
$band$ Number of Frequency Bands
$face$ Number of Cell Faces
max Domain Upper Limit
min Domain Lower Limit
$quad$ Correlated-k Quadrature Scheme
ord Number of Ordinates
sca Frequency Specific Scattering
$spec$ Number of Species
$wall$ Wall Location
ν Frequency Specific Value

I. Introduction

There is a desire to operate scramjet engines at the highest possible temperature in order to maximize the thrust that can be generated. The role of thermal radiation in the energy balance inside a combustor has been little studied and is poorly understood. Previous work studied the hydrogen-fueled HyShot II combustion chamber and found the thermal radiation to be insignificant.[1] The current work considers combustion chambers similar to the HIFiRE-2 supersonic combustor.[2,3] It is anticipated that the radiative component of wall heat flux may be higher in the HIFiRE-2 combustor due to two effects: (1) its use of hydrocarbon fuel that generates significant quantities of radiating species such as carbon dioxide that are absent from HyShot II; and (2) the HIFiRE-2 combustor is significantly larger in volume than that for HyShot II.

Radiation is evaluated using a two step approach. First, the combustion flow is computed using a turbulent RANS CFD code. These computations have already been presented in previous work by the Air Force Research Laboratory (AFRL).[3] Then, the flow-field results are used as input into radiative heat

transfer simulations. The current work uses two different approaches for simulating radiation transport: (1) a Discrete Ordinates Method, and (2) a ray tracing technique. In each case, a spectrally resolved narrow-band approximation is used as the spectral model. The narrow-band spectral approximation introduces inherent epistemic error from both the source databases used as well as from the approximations made in creating banded models.[4,5] The propagation of these errors through the radiation predictions are analyzed to place uncertainty bounds on the computed results.

The spectrally resolved thermal radiation results with their associated errors are compared to a series of experimental measurements taken at NASA Langley Research Center on a HIFiRE-2 test rig.[6]

In the following sections, the CFD and radiation methodologies are described. Then, the scramjet combustor rig and the radiation measurements are discussed. Results are then presented on the flow-field, the combustor wall heating, flow cooling, and finally comparisons between the predicted and measured radiation emissions. The paper ends with a summary and conclusions.

II. Methodology

The three-dimensional flow-field simulations are computed using a twenty-two-species chemically reacting k-ϵ RANS CFD RANS computation.[7,8]

The resulting flowfield calculations are post-processed to evaluate radiation effects using a three-dimensional Discrete Ordinates Method (DOM) code called "GRASP" and a three-dimensional Ray Tracing Method (RT).[9–11] The DOM code provides a first-order spatial solution to the Radiative Transfer Equation (RTE) and employs a simplified correlated-k narrow-band spectral model. These methods allow for both spatially and spectrally resolved solutions for radiation intensity, heat flux, absorptivity, and optical depth. The three-dimensional discretized ray tracing method provides a second-order spatial solution with a narrow-band spectral model, and it provides much better spatial and angular resolution than the DOM.[11,12] However, it only solves for one location at a time. The DOM code can take scattering and reflective boundary conditions into account, whereas the ray tracing method cannot.[10] The RT code employs an identical spectral model to that used by the DOM.

II.A. Discrete Ordinates Method for Radiative Analysis

For the three-dimensional DOM, the final CFD solution is projected onto a structured grid for which the radiative intensity is solved for a series of discrete directions at each grid-point.[9] The total spectrally resolved radiative energy flux "F_ν" to a cell face is found by integrating the total angular intensity "I_ν" contributions that are normal to the plane of the cell face. This expression is given in Eq. (1), where "μ" is the cosine of the angle "ϕ" between the ordinate and the vector normal to the plane. The coordinate system is illustrated in Fig. 1. Equation (1) can be numerically integrated based on an S_n weighting scheme.[13,14]

$$F_\nu(s) = \int_0^{2\pi} \int_0^1 I_\nu(s,\mu,\theta)\mu d\mu d\theta \tag{1}$$

The main equation for radiative intensity is the RTE which is given by Eq. (2) where the left hand side of the equation represents the change in intensity over distance, and the terms on the right hand side represent, from left to right, extinction due to absorption, extinction due to scattering, contribution due to scattering, and contribution due to emission. The term "f_ν" refers to the scattering redistribution function where the source angles (the secondary angles) are denoted by primes. The term "B_ν" denotes the frequency specific blackbody intensity as determined by the Planck distribution function.[10]

$$\frac{dI_\nu(s,\mu,\theta)}{ds} = -\frac{\kappa_{abs}(s)}{\mu} I_\nu(s,\mu,\theta) - \frac{\kappa_{sca}(s)}{\mu} I_\nu(s,\mu,\theta) + \frac{\kappa_{sca}(s)}{4\pi\mu} \int_0^{2\pi} d\theta' \int_{-1}^{1} d\mu f_\nu(s,\mu,\theta,\mu',\theta') I_\nu(s,\mu',\theta') + \frac{\kappa_{abs}(s)}{\mu} B_\nu(T(s)) \tag{2}$$

The boundary conditions at the walls are modeled as partially emissive and spectrally reflecting walls.

The high temperatures in scramjet engines prevent fuel or water droplet formation meaning that Mie scattering is not possible. Additionally, the wavelengths considered are in the infrared regime, which is not significantly affected by Rayleigh scattering.[10] Since scattering is not significant in this case, it will be

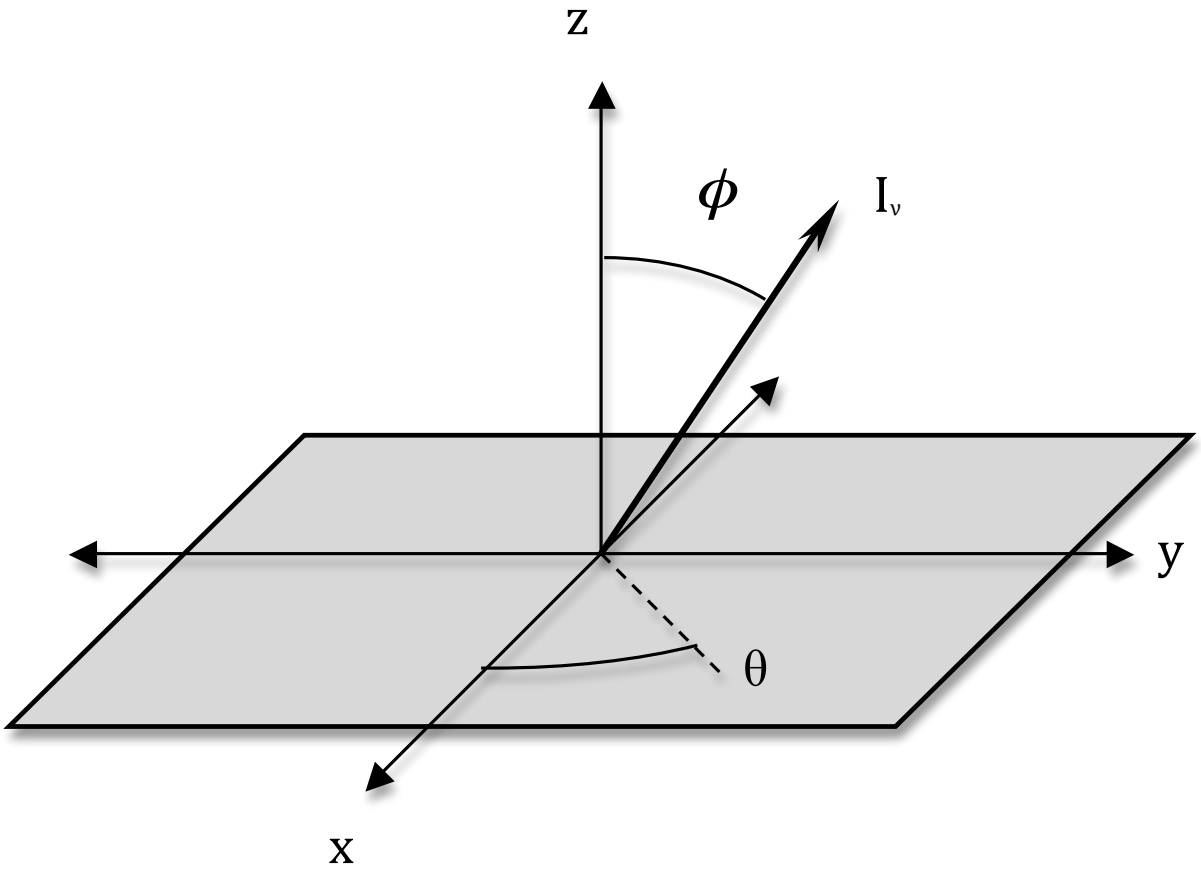

Figure 1. Angular Coordinate System

ignored in all analysis ($\kappa_{sca} = 0$) even though the DOM code is robust enough to incorporate it.[10] With this simplification, the RTE is discretized by a flux-based finite-volume scheme for multi-dimensional solvers such as GRASP resulting in Eq. (3).[9,10,15,16]

$$\sum_{m}^{N_{face}} I_\nu(m,j) \cdot a(m) = \kappa_{abs}(i) V(i) (B_\nu(i) - I_\nu(i,j)) \tag{3}$$

II.B. Ray Tracing Method for Radiative Analysis

For the purpose of verification, a second-order spatially discretized three-dimensional ray tracing method with a two-point narrow-band spectral method is employed.[11] While the selection of paths for the ray tracing method is often chosen with a Monte Carlo scheme, a pre-determined ray spacing is opted for in this application.[12] The ray tracing method divides a solid angle hemisphere into a discrete series of angles and one-dimensionally integrates the radiative heat transfer along each path until it reaches a simulation boundary. The one-dimensional integration is given by Eq. (4). The individual intensities are then integrated angularly as in Eq. (1), which can be performed numerically with Eq. (5).[11]

$$\frac{3I_\nu(i,j) - 4I_\nu 0(i-1,j) + I_\nu 0(i-2,j)}{2\Delta s(i)} = \frac{\kappa_{abs}(i)}{\mu(j)} (B_\nu(i) - I_\nu(i,j)) \tag{4}$$

$$F_\nu = \sum_{j}^{N_{ord}} I_\nu(\theta(j), \phi(j)) \sin(\phi(j)) \cos(\phi(j)) \sin(\Delta\phi(j)) \Delta\theta(j) \tag{5}$$

II.C. Spectral Model

The absorption coefficients for both the ray tracing method and the DOM are determined by a simplified two-point narrow-band correlated-k "c-k" spectral model. While detailed multi-species c-k methods are very accurate, they can require large amounts of computational time to generate all of the cell specific quantities. This time can be reduced by using pre-computed spectral tables, but these tables can be large to the point of being unusable in a realistic computational system.[17] Many simplifications to the c-k method have been developed to compromise between accuracy, time, and memory requirements.[18,19] The method chosen for this study is a narrow-band two-point gaussian c-k distribution.

All frequency-based models assume that the total flux is calculated by a frequency integration of the spectrally resolved flux as given in Eq. (6).

$$F(s) = \int_{\nu_{min}}^{\nu_{max}} F_\nu(s) d\nu \tag{6}$$

Realistic mixed-gas spectra are very complicated, with hundreds of millions of spectral lines that depend on temperature, pressure, and species concentration. The line-by-line method allows for the arbitrarily fine computation of the spectral absorptivity at any frequency.[12,19] Narrow band methods divide the absorption spectrum into bands of given width. In this case, 25 cm^{-1} wide bands are employed. Generalized absorption characteristics are then calculated for each band using the arbitrarily fine absorption spectrum as calculated by the line-by-line method. The c-k method transforms the very fine resolution absorption spectrum from the line-by-line method, into an ordered monotonic absorption spectrum, which can be approximated with a handful of quadrature points as in Eq. (7), where "g" is the quadrature weight,"l" is the quadrature index, and "k" is the spectral band index. The extreme simplification of this approach is to take a quadrature point at the statistical average of the absorption band and set the quadrature weight equal to "1" for the single point in the band.[1]

$$F(s) = \sum_{k}^{N_{band}} \sum_{l}^{N_{quad}} g(l) F_\nu(s,k,l) \Delta\nu(k) \tag{7}$$

A step up from a band-averaged approach would be to choose two equally weighted quadrature points ($g = 0.5$) at one standard deviation above and below the mean band absorptivity. A true c-k method would require the reordering of the absorption spectrum of each band and numerically calculating the weighted value for both standard deviation locations. A simplified method involves setting the quadrature point values as those of the standard deviations in the error function as in Eq (8) where "$\bar{\kappa}$" is the band-averaged absorption and "σ" is the band standard deviation.

$$\kappa_\nu(s,l) = \bar{\kappa}_\nu(s) \left(ERF \frac{\pm\sigma_\nu(s)}{\bar{\kappa}_\nu(s)} + 1 \right) /2 \tag{8}$$

Because all bands are assumed independent, the total integration can be computed as the sum of the spectrally resolved flux multiplied by the bandwidth for each frequency as in Eq. (7). However, the quadrature points within the sub-band are not necessarily independent, but all information as to their cross-correlation is lost when these methods are applied. Therefore, the quadrature absorption values are assumed to have no cross-correlation with the other quadrature points in their own band, and they are assumed to have perfect correlation with the same quadrature points for absorption values at other locations.

The calculation of absorption coefficients is performed with a line-by-line calculation for all species of interest (water vapor, carbon dioxide, the hydroxyl radical, and carbon monoxide) at representative pressures and temperatures pertinent to the conditions inside a scramjet. The individual lines are extracted from the HiTemp database using JAVAHAWKS, at a pressure of 2 Atm and temperatures of 600, 1000, 1500, 2000, 2500, and 3000 K, respectively.[4] The extracted lines are then used to calculate a series of optical depths for each species at each temperature with a resolution of 0.001 cm^{-1}. These high-resolution calculations are then used to create the band statistic needed for the spectral model, resulting in a series of fast spectral lookup tables for each species. The lookup tables can be used to directly evaluate the species absorption as in Eq. (9), where "n" denotes the species index, "S_ν" denotes the species absorptivity interpolated from the table, "$X(i,n)$" represents the mole fraction, and "$\rho_n(i)$" represents the relative number density normalized to number densities used to calculate the lookup tables.

$$\kappa_\nu(i,l) = \sum_{n}^{N_{spec}} S_\nu(T(i),n,l)X(i,n)\rho_n(i) \tag{9}$$

II.D. Error Propagation

With the use of a spectral model, a means of estimating the epistemic uncertainty of the absorption coefficients stemming from the spectral tables becomes necessary, as does predicting the error from the modeling approximation. The simplest means of determining the potential error contributions is a differencing scheme. In order to estimate the modeling error, a one-dimensional unit problem is employed. The problem compares a high spectral resolution and a low spectral resolution calculation of the total heat flux within each band as given by Eq. (7). The high-resolution band treats each of the high-resolution optical depths, as calculated by the line-by-line extraction, as equally weighted quadrature points, resulting in 2500 equally-spaced quadrature points for each 25 cm^{-1} band. The low-resolution band employs two quadrature points per band as calculated by Eq. (8). These two methods are then compared in order to calculate the error as given in Eq. (10), where "E_ν" represents the band-specific dimensionless error. Additionally, a factor of experimental uncertainty from the HiTemp databases is added in Eq. (10) as "E." Since each individual line of the HiTemp database has its own associated experimental uncertainty, a general assumption of $E = 10$ % is employed for all bands.

$$E_\nu(k) = abs\left(\frac{F_{\nu,low}(k)}{F_{\nu,high}(k)}\right) + E \tag{10}$$

The unit problem is homogeneous, which means that fluxes for each quadrature point can be calculated using Beer's law as shown in Eq. (11) as opposed to a more complicated DOM or RT method.[10]

$$F_\nu(k,l) = B_\nu(T,k,l)\left(1 - e^{-\kappa_\nu(k,l)\Delta s}\right) \tag{11}$$

The predicted errors are tabulated for the representative unit problem of pressure equal to 2 Atm and path length equal to 0.10 m. The errors are found individually for water vapor, carbon dioxide, the hydroxyl radical, and carbon monoxide, each with a mole fraction of 0.10. The calculations are repeated for each 25 cm^{-1} band ranging from 50-8000 cm^{-1} (200-1.25 microns). The calculations are also repeated for the 6 temperatures of 600, 1000, 1500, 2000, 2500, and 3000 K, resulting in a three-dimensional predicted error table with 4 species, 6 temperatures, and 319 bands. These are the same dimensions as the absorptivity tables.

With the absorption and uncertainty tables calculated, the uncertainty of a full simulation can be quantified. The method employed is a differencing scheme, wherein the physical domain is solved for each spectral quadrature point using either the DOM (Eq. (3)) or the RT method (Eq. (5)) and spectrally integrated using Eq. (7). The scheme is then repeated with the absorption tables either multiplied or divided by the error tables. The resulting differences in radiative heat flux are taken as the epistemic uncertainty of the system as given by Eq. (12), where "U" is the dimensionless uncertainty factor.

$$U(s) = \frac{\Delta F(s)}{F_0(s)} - 1 \tag{12}$$

II.E. Computational Fluid Dynamics

The input data for the radiative simulations codes are Computational Fluid Dynamics (CFD) simulation results. The CFD results are performed at the AFRL using the CFD++ code with a $k-\epsilon$ RANS solver. The chemical mechanism is a 22 species combustion model as developed by Wang and Laskin.[20] Further details of the mechanisms and solvers can be found in the original publication of the CFD simulations by Storch et al.[3]

The specific simulation of interest is intended to duplicate the conditions of a Mach 6.5 flight of the HIFiRE-2 scramjet with an equivalence ratio of 1.0 for a 0.36-0.64 methane-ethylene fuel, and an oxidizer of air. The simulation is run with 1.4 million grid-points for a quarter of the domain employing planes of symmetry at both the vertical and horizontal centerlines. The full simulation domain can be seen in Fig. 2.

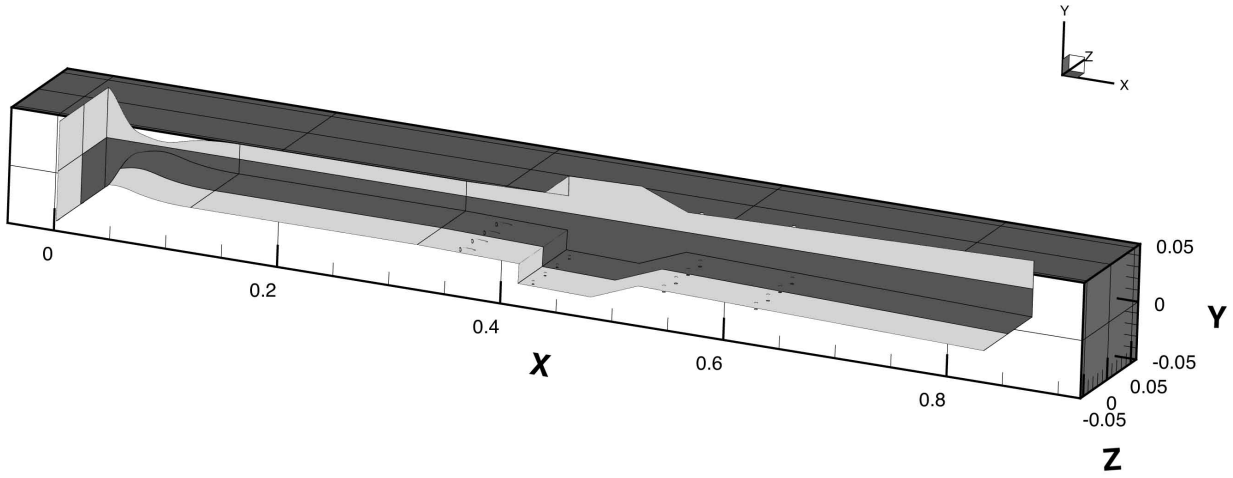

Figure 2. CFD Simulation for Mach 6.5 with 1.0 equivalence ratio: The flow is from left to right. The full facility channel is shown with the computational simulation domain darkened. The active fuel injectors are located at x = 0.363 m and x = 0.539 m . The flame holder is located at x = 0.413 m

II.F. Experimental Setup

The experimental emission measurements are made on the HIFiRE Direct-Connect Rig (HDCR) in the Arc-Heated Scramjet Test Facility (AHSTF) at NASA Langley. The HDCR is constructed and operated to provide ground-test support for Flight 2 of the HIFiRE Program using the same flowpath lines as the flight engine.[21] A two-dimensional schematic of this flowpath appears in Fig. 3.[22]

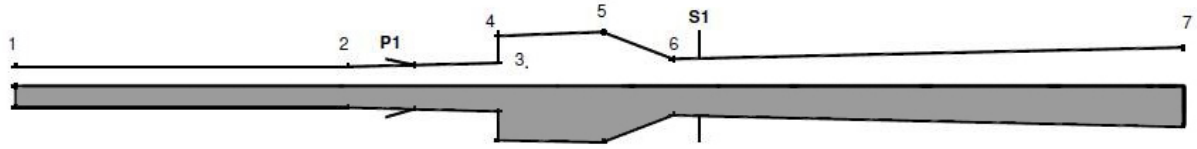

Figure 3. Schematic of flowpath: flow is left to right. Isolator extends from station 1 to 2, cavity flameholder from 3 to 6. Primary and secondary fuel injection sites are denoted by P1 and S1. Emission measurements are made at the exit of the combustor denoted as station 7. The CFD domain is denoted in gray.

An optical diagnostics flange and attendant hardware is attached to the engine at the exit of the combustor (station 7 in Fig. 3.) The primary function of the optical hardware is to execute tunable diode laser absorption measurements along 16 lines of sight across (and adjacent to) the combustor exit. Three diode lasers are sequentially tuned across multiple water spectral features in the neighborhood of 1.4 microns (7143 cm^{-1}) with the aim of determining the temperature and water concentration fields at the exit plane.[6] The absorption measurements are conducted in such a way that for every 1 ms of data collection, approximately 100 microseconds of signal due just to the nascent hot gas emission is also collected and that is what we report here. The emission signals are captured using InGaAs photodetectors with a narrow spectral bandwidth of 1.1-1.8 microns (5556-9091 cm^{-1}). A silicon filter removed emission at wavelengths below 1.1 microns (9091 cm^{-1}). (The filter is necessary to maintain good signal-to-noise ratios in the absorption measurements.) A photograph of the optical hardware attached to the HDCR is shown in Fig. 4. Sixteen photodetectors and associated transimpedance amplifiers are split between two electronics boxes one positioned on the body (top) side of the combustor exit and one on the port (left) side of the combustor exit. This arrangement

permits collection of the emission from 8 vertical views and 8 horizontal views that share some common overlap with respect to their solid angles of emission collection. In Fig. 5, we show a scaled schematic of the location of the 16 individual photodetectors with respect to the combustor exit which is 0.05 m tall and 0.10 m wide. Apertures located between the photodetectors and combustor exit limited the solid angle of light collection. Specific values of the light collection (field of view and sheet thickness) for each photodetector are noted in Table 1 below.

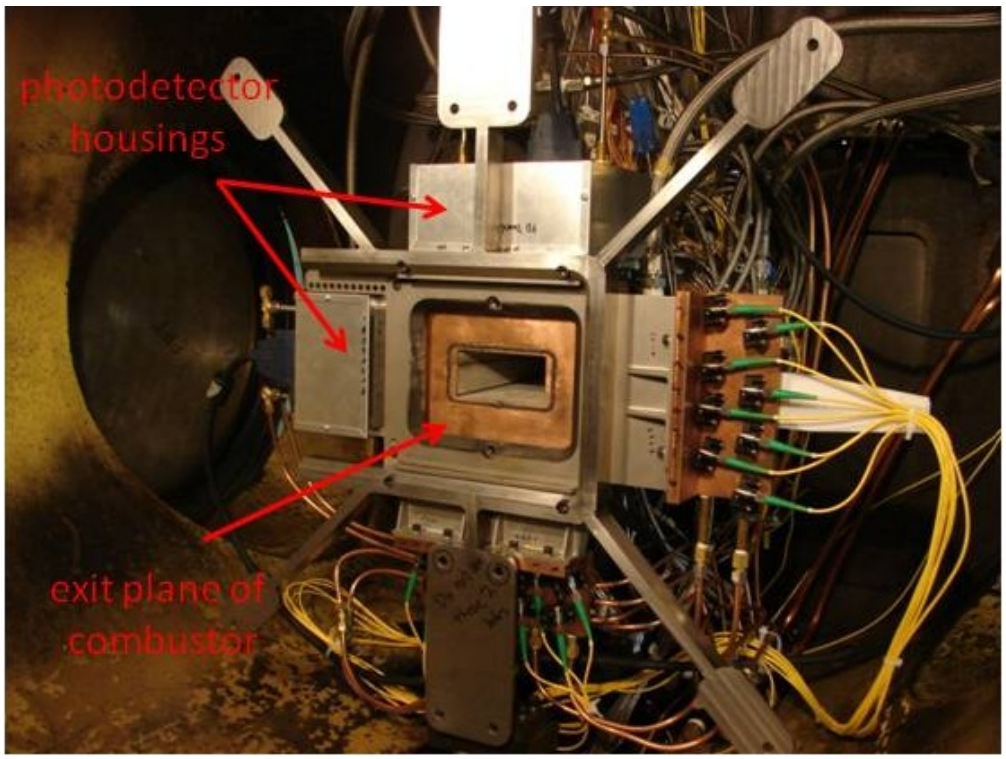

Figure 4. Optical hardware mounted to the exit plane of the HDCR combustor. The 16 photodetectors used in the emission measurements are located in two housings as indicated. (Flow is right to left.)

III. Results

First, a brief description of the CFD simulations is presented. There, additionally, the results include a comparison of different radiative simulation techniques, an analysis of the variation of radiative wall heat flux due to spectral model uncertainty, and a preliminary prediction of the effects of radiative cooling on the flowfield is presented. Finally, a comparison between experimental and simulated radiative heat flux measurements is provided.

III.A. Computational Fluid Dynamics results

The computational results for the simulation of a Mach 6.5 flight of the HIFiRE-2 scramjet with an equivalence ratio of 1.0 for a 0.36-0.64 methane-ethylene fuel are given in Figs. 6 and 7. The temperatures peak in the flame holder around 2800 K and the pressure peaks at the flame holder exit at 350 kPa. The density during combustion is generally less than 1 kg/m^3. The Mach number is generally above 1 for most of the flow except for the locations by the sidewalls and in the flame holder.

The mass fractions of the combustion products show the general flame profile and propagation. Most combustion products form directly downstream of the injection ports and do not spread throughout the entire chamber before exiting. This implies that combustion only takes place in narrow columns. Additionally, it is shown in Fig. 7 that carbon monoxide does not make its way into the flame holding cavity, and the hydroxyl radical does not spread much beyond the flame boundary. These observations may have a large impact on the radiative analysis.

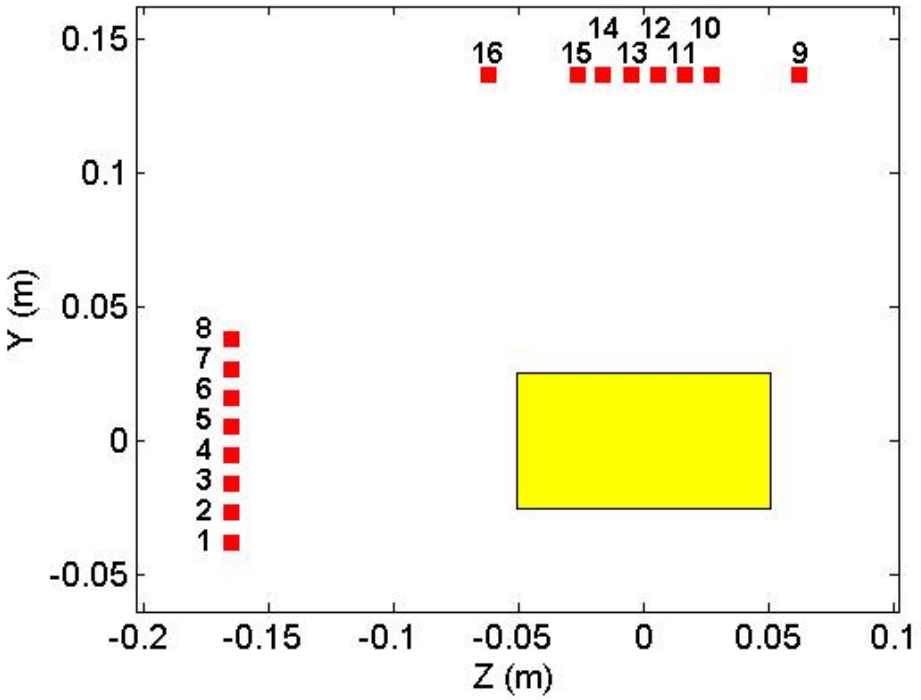

Figure 5. Location of the emission photodetectors with respect to the exit of the combustor shown in yellow. Flow is out of the page.

III.B. Radiative Heat Flux and Uncertainty

The radiative wall heat fluxes are calculated with the DOM program "GRASP" employing a 97,061 grid-point S_8 solver. The spectral model employed is a two-point band model, as described above, ranging from wavenumbers of 50 to 8000 cm^{-1} (200 to 1.25 micron) with bandwidths of 25 cm^{-1} resulting in 319 individual bands. The centerline boundary conditions are assumed to be symmetry planes, whereas the side walls are assumed at all frequencies to have absorptivity, reflectivity, and emissivity of 1.0, 0.0, and 0.0, respectively. The reasoning behind these characteristics is that only the net radiative heating to the wall is of concern for the current comparisons. The total radiative heat flux to the side walls is given in Fig 8 (a).

The peak radiative heat flux of 56 kW/m^2 is located along the sidewall of the flame holding cavity with other hot regions on the bottom and top of the cavity. The radiative heat flux uncertainty resulting from the uncertainty in the spectral model as calculated by Eq. (12) is given in Fig. 8 (b). The peak uncertainty of 15 % (+8/-7 %) is located near the wall on the top and bottom plates at the combustion chamber exit where radiative wall heat flux is at a minimum. One important note is that the input error tables have a minimum uncertainty of ±10 % meaning that the sensitivity to the spectral tables reduces the error as it propagates through the system.

The implication of these results is that the uncertainties stemming from the spectral model are generally higher in the areas of lower heat flux. Part of this comes from the error tables having a smaller value as the temperature rises. With the higher temperatures in the flame holder, the uncertainty is reduced. Additionally, the areas of the highest relative uncertainty for the radiative wall flux tend to be areas of a higher relative concentration of minor species such as carbon monoxide and the hydroxyl radical as opposed to water and carbon dioxide. The two-point spectral model employed calculates the input uncertainty, "U," to be much higher for minor species than for major species. The reason behind this uncertainty is that the individual bands of the minor species have a much greater variation than those of the major species resulting in the 2-point approximation being less able to accurately capture the band characteristics. Additionally, the relative uncertainty in the model tends to be lower at higher temperatures. Thus, the high temperature flame holder region has lower uncertainty. However, because the overall radiative heat flux to the wall is considerably higher in the flame holder and along the centerline of the side-walls, the absolute uncertainty

Table 1. Position and field of view of photodetectors at the exhaust port, x = 0.83 m

Sensor Number	Orientation	Field of View (deg)	Sheet Thickness (deg)	Y-Position (m)	Z-Position (m)
1	Horizontal	43.8	1	-0.038	0.168
2	Horizontal	38.3	1	-0.027	0.168
3	Horizontal	12.7	1	-0.016	0.174
4	Horizontal	12.7	1	-0.005	0.174
5	Horizontal	12.7	1	0.005	0.174
6	Horizontal	12.7	1	0.016	0.174
7	Horizontal	38.3	1	0.027	0.168
8	Horizontal	43.8	1	0.038	0.168
9	Vertical	54.2	1	0.139	0.062
10	Vertical	12.7	1	0.146	0.027
11	Vertical	12.7	1	0.146	0.016
12	Vertical	12.7	1	0.146	0.005
13	Vertical	12.7	1	0.146	-0.005
14	Vertical	12.7	1	0.146	-0.016
15	Vertical	12.7	1	0.146	-0.027
16	Vertical	54.2	1	0.139	-0.062

is highest in those regions.

An additional form of uncertainty is the numerical uncertainty stemming from the DOM and in the forms of the spatial mesh and angular discretization schemes employed. A more reliable approach is the ray tracing method. However, unlike DOM, the RT method does not allow for a complete field solution.

The RT method is employed at nine discrete points along the sidewalls of the domain, including three in the flame holder (x = 0.447 m), three directly downstream of the flame holder (x = 0.537 m), and three downstream of all injector ports (x = 0.687 m). The calculations are performed with 1,296 rays for each point (5 degree spacing) with a grid spacing along the trace of 0.0005 m. The detailed locations and heat fluxes as well as the comparisons to the DOM results are given in Table 2.

Table 2. Position and radiative heat flux as predicted by DOM and RT methods

x (m)	y (m)	z (m)	F_{DOM} kW/m^2	F_{RT} kW/m^2	$\frac{F_{DOM}-F_{RT}}{F_{RT}}$ %
0.447	-0.033	0.025	49.3	53.7	-8.2
0.447	-0.033	0.013	48.9	52.2	-6.3
0.447	-0.010	0.051	53.7	49.0	9.5
0.537	-0.018	0.025	37.2	37.5	-0.9
0.537	-0.018	0.013	31.6	31.4	0.9
0.537	-0.004	0.051	46.7	47.5	-1.7
0.687	-0.021	0.025	36.6	37.3	-2.1
0.687	-0.021	0.013	36.5	36.5	-0.2
0.687	-0.004	0.051	40.7	40.5	0.4

As can be seen in Table 2, the DOM produces agreement within 10 % the RT method, and it follows the same trends as the RT method. The RT method and DOM tend to have closer agreement in the region downstream of the flame holder. Errors in the flame holder may be up to 9.5 %. An error of this magnitude is consistent with other studies which find that DOM can have local areas of high numerical error due to geometric effects.[23]

A grid refinement study is performed on two simulations increasing the number of points from 31×31×101 to 31×31×201 and 61×61×101 points, respectively. An angular grid refinement study ranged from the 80 point S_8 scheme to a 256 and 400 ordinate scheme for two separate simulations.

A refinement study of the RT method showed that the numerical method is properly converged.

These higher levels of refinement lower the maximum difference between the DOM and RT to 7 %. The values of the average cell intensities changed by less than 1 % with the spatial refinement and less than 0.5 % with angular refinement.

III.C. Convective and Radiative Heat Transfer

The convective heat transfer is calculated from the CFD solution and given in Fig. 9 (a). A relative comparison between the convective and radiative heat fluxes is given in Fig. 9 (b). The peak convective heating is located at the downwind lip of the flame holder. The maximum heat flux is 3.4 MW/m^2, and the minimum is negative due to the cooling at the fuel injection ports peaking around 0.3 MW/m^2.

The radiative heat flux tends to be around 2 to 10 % of the convective heat flux in the flame holder and 1 to 3 % of the convective heat flux downstream of the flame holder. The notable spikes in the data(as seen in Fig. 9 (b)) are around the injector ports where the cold fuel is causing a strong convective cooling effect compared to the radiative heating. These relative numbers are significantly higher than the convective and radiative comparisons of the HyShot II, and they may justify incorporating the wall radiative heat flux into further CFD simulation of the HIFiRE-2 combustion chamber.[1] A final note is that with the uncertainty mentioned in the previous section, the relative heat fluxes range from 1 to 3 % and 8 to 12 % (depending on location) of the total convective heat flux. This means that radiative heat flux will still be a significant factor in wall heating regardless of its uncertainty.

III.D. Flow Cooling

An additional concern is whether or not it is necessary to couple the radiative solver directly to the CFD solver. The literature differs on the extent of the effects of direct coupling depending on the extent of the necessity for flow coupling depending on the test case. In some cases with a high amount of radiative material, the temperature change has been found to be as much as 20 K due to the coupling effects of radiation.[24] However, in cases such as the HyShot II scramjet combustor, the temperature changes are found to be on the order of 3 K due to radiation.[1]

The volumetric radiative cooling for the HIFiRE-2 combustor is shown in Fig. 11. The flow is both heated and cooled by thermal radiation. The thermal heating takes place in areas where the flow has not undergone any combustion, such as the center of the channel and near the fuel injectors. The magnitude of thermal heating is on the order of 1.1 MW/m^3 in very small regions, whereas the thermal cooling can be up to 5 MW/m^3 over significantly larger regions. This suggests that, while there is flow-to-flow radiative cooling taking place, the majority of the radiative cooling of the flow is absorbed by the chamber wall, which is modeled using an absorptivity, reflectivity, and emissivity of 1.0, 0.0, and 0.0, respectively, for all frequencies.

In order to investigate the effects of radiative cooling on the flow, a post-processing analysis is performed on the CFD solution. A series of stream-traces is taken from the CFD solutions, with the predicted volumetric cooling rate, "Q", from the radiative solutions projected onto the stream traces. The traces are then integrated using Eq. (13) to find the predicted change in temperature due to radiative cooling, where "ΔT" is the predicted change in fluid temperature, "c_v" is the specific heat capacity at constant volume, "ρ" is the density, "v" is the stream-wise velocity, and "s" is the stream-wise location.

$$\Delta T = \int_{s_{min}}^{s_{max}} \frac{Q(s)}{c_v(s)\rho(s)v(s)} ds \tag{13}$$

Employing this method demonstrates that temperature can change due to radiation from a negligible 2 K up to a significant 245 K depending on the stream-trace, with an average temperature reduction of 41 K for all stream traces taken. The effect of the epistemic spectral uncertainty could change the overall temperature reduction by up to ±8 %. The averaged temperature reduction uncertainty is ±7 %. This temperature change prediction is far greater than those of previous works on radiatively cooled supersonic flows.[1,24] The explanation for the discrepancy lies in the fact that the prior test cases had geometries without any cavity flame holders and, as such, were without recirculation zones. The current test case has

significant recirculation zones in the flame holder as shown in Fig. 11. The fluid elements that follow the streamlines into the flame holding cavity, such as the black trace in Fig. 11, are able to be cooled by 15-245 K before exiting the combustor due to their residence times of 4 to 39 milliseconds. However, when the fluid element is not recirculated in the flame holding cavity, such as the red trace in Fig. 11, the residence time of the element is only 0.7-1.2 milliseconds, resulting in a temperature change of 2 to 7 K, depending on the individual flow-path.

Since radiative wall heating is assumed to be the main source of radiative flow cooling, an additional simulation is run with the walls with all frequencies having an absorptivity, reflectivity, and emissivity of 0.5, 0.5, and 0.5, respectively. The resulting relative change in flow cooling is shown in Fig. 12. The net volumetric flow cooling is generally reduced with an increase in wall reflectivity and emissivity. The cooling along specific streamlines reduces by an average of 37 %, and the peak flow cooling for all stream-traces is reduced from 245 K to 159 K. These values are still non-negligible.

The main implication of large changes in temperature in the flowfield due to radiative cooling is justification of the direct coupling of the radiative solver to the CFD solver when a cavity flame holder is utilized in a scramjet engine. Such couplings with variations in wall boundary conditions will be addressed in future work.

III.E. Experimental Assessment

As described earlier, thermal radiation over a narrow infrared band is measured in the exhaust nozzle of the experimental test rig. Using the setup on the HDCR in the AHSTF at NASA Langley Research Center described above, the infrared signal is measured from 1.1 to 1.8 microns (5556 to 9091 cm^{-1}) and averaged over a 0.25 second window. The relative photodetector response is greater than 70 % between 6061 and 9091 cm^{-1}). Each reported signal is corrected for intrinsic electronic noise. The averaged results are normalized by their mean and given in Fig. 13 (a).

For comparison, the radiative heat flux is simulated using the RT method. For each sensor, the simulation point is given the same location and field of view as the experimental sensor. The angular spacing is 0.5 degrees with a line resolution of 0.0005 m. The spectral range of the interest is 98 bands ranging from 5550 to 8000 cm^{-1} (1.25 to 1.8 microns) with bandwidths of 25 cm^{-1}. This is less than half of the total wavenumber range simulated as illustrated in Fig. 14. This band, also, only covers a small amount of the integrated radiative heat flux for the simulation, which is approximately 5 % of the total radiative heat flux. The shorter wavelengths (less than 1.25 microns) are omitted from the simulation as the spectral bands for the molecules of interest are significantly weaker at those frequencies. The simulation results are integrated over the spectral range of interest and included in Fig. 13 for comparison, with the axis appropriately scaled for a relative comparison to the experimental data.

As can be seen in Fig. 13 (a), the horizontal simulation data (sensors 1-8) have a significantly wider range of variation than does the horizontal experimental data, whereas the vertical simulation data (sensors 9-16) has about an equal range of variation to that of the horizontal experimental data. Additionally, the simulation data is clearly symmetric for each set, whereas the experimental data is notably asymmetric.

One important reason for this difference is that the experimental flowfield is asymmetrical as demonstrated in a previous publication.[6] The CFD simulation, however, is assumed symmetrical about both axes.

Another issue is that the experimental flow conditions are known to have a temporal variation as indicated by the 10 % error bars. As such, the simulations would need to incorporate such variations as well. Incorporating these variations would be to effectively include any aleatory flowfield uncertainty. With the flowfield fixed for the simulations (as it is at the moment), the distribution of radiative heat fluxes is essentially fixed. Future work may allow the simulated flowfield to vary, resulting in a change in radiative distribution. As such, the trends may overlap when that variation is incorporated.

Additionally, as these are strictly preliminary results, the data points may still be in good agreement in a quantitative sense, but without absolute experimental heat flux data from the sensors, this cannot be confirmed. One trend that is apparent is that in both cases, the sensors with the widest field of view tend to have higher relative heat flux as opposed to the sensors with narrower fields of view.

The variations in the simulations due to the uncertainty in the spectral model are shown in Fig. 13 (b). Since all points from the simulation rely on the same spectral model, the spectral uncertainty factor works essentially as a linear multiplier in this optically thin case causing the results to scale as a group. The varied simulations are also shown in Fig. 13 (b) and display a maximum and minimum group scaling of 111 % and 90 %, respectively, due to uncertainty, but the shape of the curve does not undergo any relative change due

to the uncertainty incorporation. This uniform scaling is due to simple geometry and low optical depth at the exit plane.

These uniform scaling effects at the exit are different from the full flowfield DOM results as given in Fig. 8 (b), which predict a notable change in relative radiative wall heat flux due to uncertainty depending on location. The reason behind this difference is that the full DOM simulation takes into account a wider spectral range that can have significantly higher optical depths. Whereas, the frequencies simulated for the exit plane comparison are optically thin. Radiation propagation more nonlinearly at higher optical depths, which means that changes due to uncertainty will not uniformly propagate throughout the system. Additionally, the exit plane simulations are geometrically simpler and unobstructed compared to the full DOM simulation. This means that the geometry in the DOM analysis may obstruct the uncertainty propagation for the full simulation and cause non-uniformities.

IV. Conclusion

Flow in the HIFiRE-2 combustor was modeled using a $k-\epsilon$ RANS simulation. Radiative heat transfer was subsequently modeled using spectrally resolved narrow-band DOM and ray tracing method simulations. The CFD simulation predicted the convective heat flux to be on the order of 1.0 to 3.4 MW/m^2, mainly concentrated around the flame holder. The radiative heating was found by the DOM code to be from 11 to 56 kW/m^2 resulting in a radiative to convective heating ratio of 1 to 10 % depending on location, the highest relative heating being in the flame holder.

The effect of the uncertainty in the spectral model on the DOM results was found to range from +6/-5 to +8/-7 % of the overall radiative heating depending on location. The highest uncertainty was in the downstream regions with higher concentrations of minor species, lower temperatures, and lower radiative heat fluxes than in the flame holder. Additionally, the DOM was compared to a much more rigorous ray tracing method and was found to have a numerical error of up to ±10 % in the flame holder with errors of less than ± 1 % in other locations.

The radiative cooling of the flow was examined using a series of stream-traces in the flowfield and calculating the integrated heat loss along each one. The flow was found to cool negligibly for traces that did not pass though the flame holder. However, traces that were caught in the recirculation zone of the flame holder were found to cool by up to 245 K.

The thermal radiation at the exhaust port was measured experimentally using an array of infrared photo-detectors on the HDCR in the AHSTF at NASA Langley Research Center. The emissions at these same measurement locations were also simulated using a ray tracing radiative heat transfer code. The results showed that the symmetric CFD simulation displayed no strong correlation with the experimental measurements. However, the future incorporation of aleatory uncertainty in the simulations and absolute values in the experimental data may result in closer agreement.

Future work will include a direct comparison of the measured radiative heat flux to the simulated radiative heat flux for use in quantitative evaluation of the simulations. Additionally, the validity of the error tables used to predict the spectral uncertainty will be more thoroughly investigated to determine the limits of applicability when predicting epistemic uncertainty. Finally, reasonable flowfield variations will be necessary to fully predict the uncertainty of the simulations.

Long-term future work will include a coupling of the CFD code to the DOM radiative transfer code in order to directly incorporate both wall heating and flow cooling into the simulations.

Acknowledgments

The experimental work was supported in part by Advanced Propulsion Test Technology (Ed Tucker, Executing Agent) and the Air Force Office of Scientific Research (John Schmisseur, Program Manager).

The authors would also like to thank Adam Irvine for providing use of his research codes.

This material is based upon work supported by the Department of Energy [National Nuclear Security Administration] under Award Number NA28614.

its use would not infringe privately owned rights. Reference herein to any specific commercial product, process, or service by trade name,trademark, manufacturer, or otherwise does not necessarily constitute or imply its endorsement, recommendation, or favoring by the United States Government or any agency thereof. The views and opinions of authors expressed herein do not necessarily state or reflect those of the United States Government or any agency thereof.

References

[1]Crow, A., Boyd, I., and Terrapon, V., "Radiation Modeling of a Hydrogen-Fuled Scramjet," No. 2011-3769 in 42nd AIAA Thermophysics Conference, AIAA, Honolulu, HI, June 2011.

[2]Gruber, M., Smith, S., and Mathur, T., "Experimental Characterization of Hydrocarbon-Fueled, Axisymmetric, Scramjet Combustor Flowpaths," No. 2011-2311 in 17th AIAA International Space Planes and Hypersonic Systems and Technologies Conference, AIAA, San Francisco, CA, April 2011.

[3]Storch, A. M., Bynum, M., Liu, J., and Gruber, M., "Combustor Operability and Performance Verification for HIFiRE Flight 2," No. 2011-2249 in 17th AIAA International Space Planes and Hypersonic Systems and Technologies Conference, AIAA, San Feransisco, CA, April 2011.

[4]Rothman, L., Gordon, I., Dothe, R. B. H., Gamache, R., Goldman, A., Perevalov, V., Tashkun, S., and Tennyson, J., "HITEMP, The High-Temperature Molecular Spectroscopic Database," *Journal of Quantitative Spectroscopy and Radiative Transfer*, Vol. 111, 2010, pp. 2139–2150.

[5]Liu, L., Tan, H., and He, Z., "Inverse Radiation Problem of Source Term in Three-Dimensional Complicatd Geometric Semitransparent Media," *International Journal of Thermal Sciences*, Vol. 40, 2001, pp. 528–538.

[6]Brown, M. S., Herring, G. C., Cabell, K., Hass, N., Barhorst, T. F., and Gruber, M., "Optical Measurements at the Combustor Exit of the HIFiRE 2 Ground Test Engine," No. 2012-0857 in 50th AIAA Aerospace Sciences Meeting including the New Horizons Forum and Aerospace Exposition, AIAA, Nashville, Tennessee, January 2012.

[7]Liu, J. and Gruber, M., "American Institute of Aeronautics and Astronautics This material is declared to be a work of the U.S. Government and is not subject to copyright protection in the United States. Preliminary Preflight CFD Study on the HIFiRE Flight 2 Experiment," No. 2011-2204 in 17th AIAA International Space Planes and Hypersonic Systems and Technologies Conference, AIAA, San Fransisco, CA, April 2011.

[8]Pope, S. B., *Turbulent Flows*, Cambridge University Press, New York, 2000.

[9]Chandrasekhar, S., *Radiative Transfer*, Dover Publications Inc, New York, 1960.

[10]Liou, K. N., *An Introduction to Atmospheric Radiation*, Academic Press, San Diego, 2nd ed., 2002.

[11]Coelho, P. J., Perez, P., and El Hafi, M., "Benchmark Numerical Solutions For Radiative Heat Transfer in Two-Dimensional Axisymmetric Encolsures with Nongray Sooting Media," *Numerical Heat Transfer, Part B*, Vol. 43, 2003, pp. 425–444.

[12]Modest, M. F., *Radiative Heat Transfer*, Academic Press, San Diego, 2nd ed., 2003.

[13]Fiveland, W. A., "Discrete Ordinate Methods for Radiative Heat Transfer in Isotropically and Anisotropically Scattering Media," *Journal of Heat Transfer*, Vol. 109, August, 1987, pp. 809–812.

[14]Fiveland, W. A., "Three-Dimensional Radiative Heat-Transfer Solutions Three-Dimensional Radiative Heat-Transfer Solutions by the Discrete-Ordinates Method," *Journal of Thermophysics and Heat Transfer*, Vol. 2, No. 4, October, 1988, pp. 309–316.

[15]Liu, J., *GRASP: A General Radiation Simupaltion Program User's Manual*, Engineering Sciences Inc., WPAFB, OH 45433-0630, 2nd ed., December, 1997.

[16]Joseph, D., El Hafi, M., Fournier, R., and Cuenot, B., "Comparison of Three Spatial Differencing Schemes in Discrete Ordinates Methods Using Three-Dimensional Unstructured Meshes," *International Journal of Thermal Sciences*, Vol. 44, April, 2005, pp. 851–864.

[17]Wang, A. and Modest, M. F., "High-Accuracy, Compact Database of Narrow-Band k-Distributions for Water Vapor and Carbon Dioxide," *Journal of Quantitative Spectroscopy and Radiative Transfer*, Vol. 93, 2005, pp. 245–261.

[18]Pal, G. and Modest, M. F., "A Narrow Band-Based Multiscale Multigroup Full-Spectrum k-Distribution Method for Radiative Transfer in Nonhomogeneous Gas-Soot Mixtures," *Journal of Heat Transfer*, Vol. 132, February 2010.

[19]Modest, M. F. and Riazzi, R. J., "Assembly of full-spectrum k-distributions from a narrow-band database; effects of mixing gases, gases and nongray absorbing particles, and mixtures with nongray scatterers in nongray enclosures," *Journal of Quantitative Spectroscopy and Radiative Transfer*, Vol. 90, 2005, pp. 169–189.

[20]Wang, H. and Laskin, A., "A Comprehensive Kinetic Model of Ethylene and Acetylene Oxidation at High Temperature," Internal report for an afosr new world vista program, AFOSR, 1998.

[21]Cabell, K., Hass, N., Storch, A., and Gruber, M., "HIFiRE Direct-Connect Rig (HDCR) Phase I Scramjet Test Results from the NASA Langley Arc-Heated Scramjet Test Facility," No. 2011-2248 in 17th AIAA International Space Planes and Hypersonic Systems and Technologies Conference, AIAA, San Francisco, CA, April 2011.

[22]Jackson, K. R., Gruber, M. R., and Buccellato, S., "HIFiRE Flight 2 Overview and Status Update 2011," No. 2011-2202 in 17th AIAA International Space Planes and Hypersonic Systems and Technologies Conference, AIAA, San Fransisco, CA, April 2011.

[23]Joseph, D., Perez, P., and El Hafiand Bénédicte Cuenot, M., "Discrete Ordinates and Monte Carlo Methods for Radiative Transfer Simulation Allied to Computational Fluid Dynamics Combustion Modeling," *Journal of Heat Transfer*, Vol. 131, No. 052701, May 2009, pp. 052701–1 052701–9.

[24]Ghosh, S., Friedrich, R., Pfitzner, M., Stemmer, C., Cuenot, B., and El Hafi, M., "Effects of Radiative Heat Transfer on the Structure of Turbulent Supersonic Channel Flow," *Journal of Fluid Mechanics*, Vol. 677, 2011, pp. 417–444.

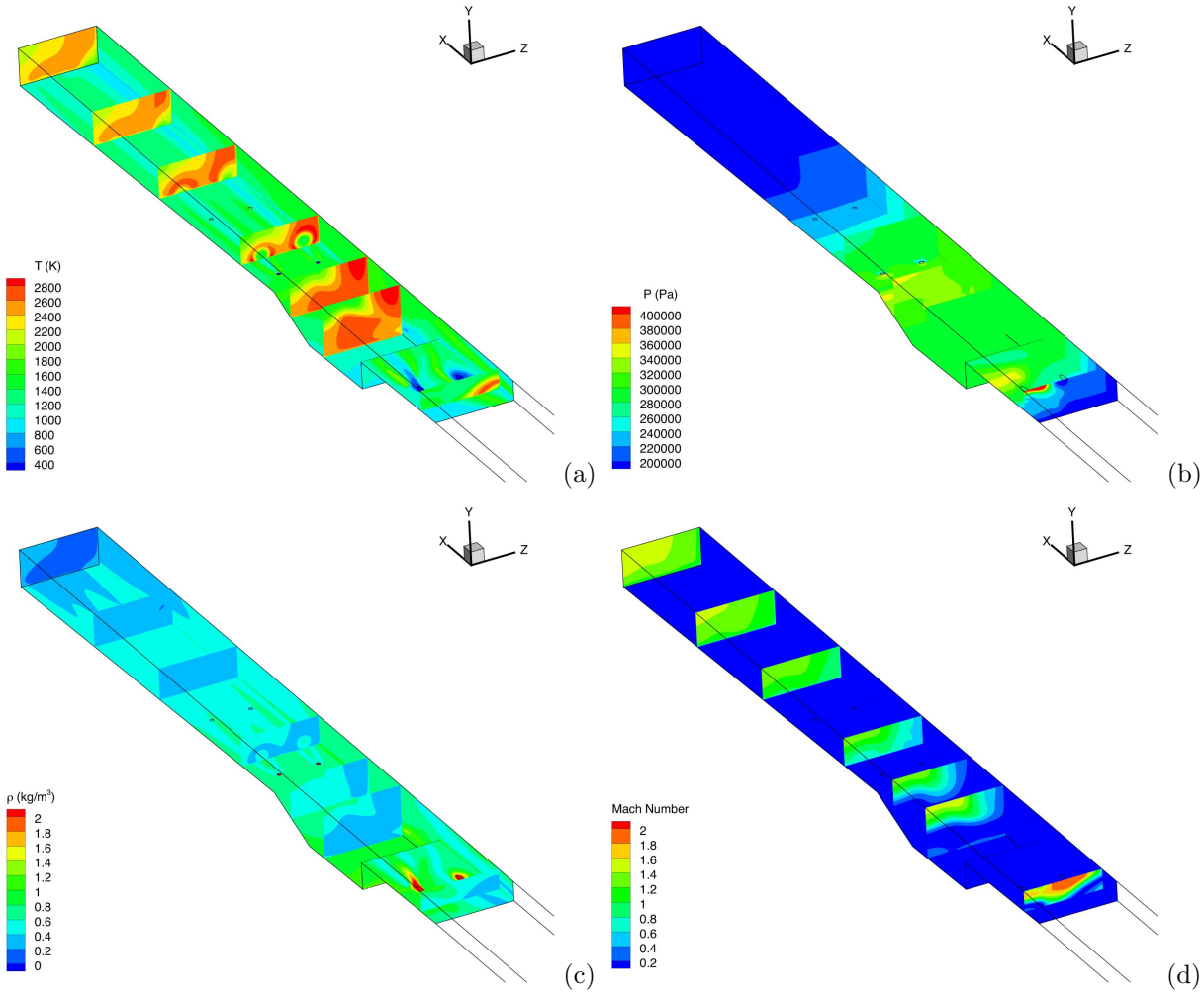

Figure 6. Temperature (a), pressure (b), density (c), and Mach number (d) from the CFD simulation

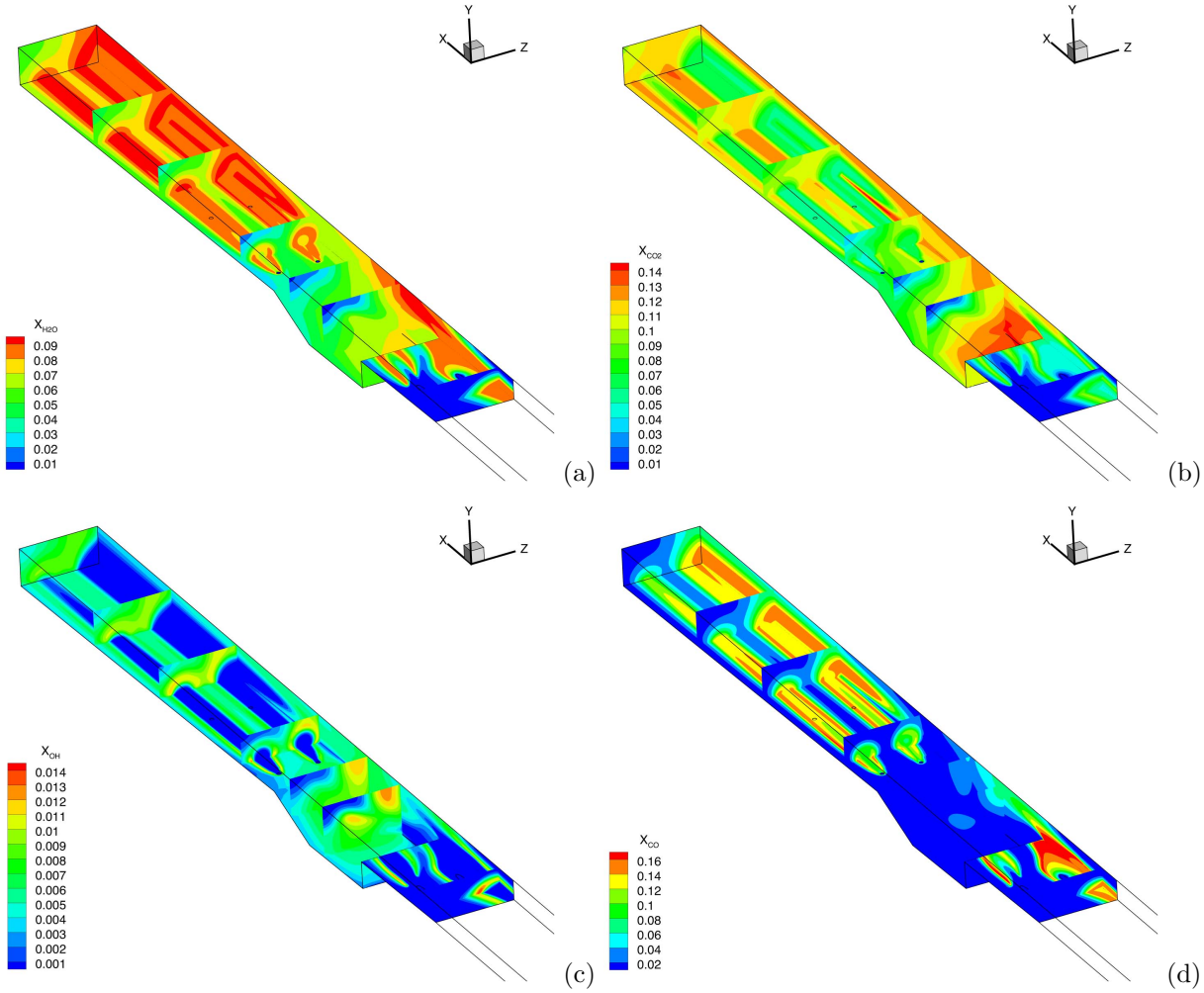

Figure 7. Mass fractions of water vapor (a), carbon dioxide (b) hydroxyl (c) and carbon monoxide (d) from the CFD simulation

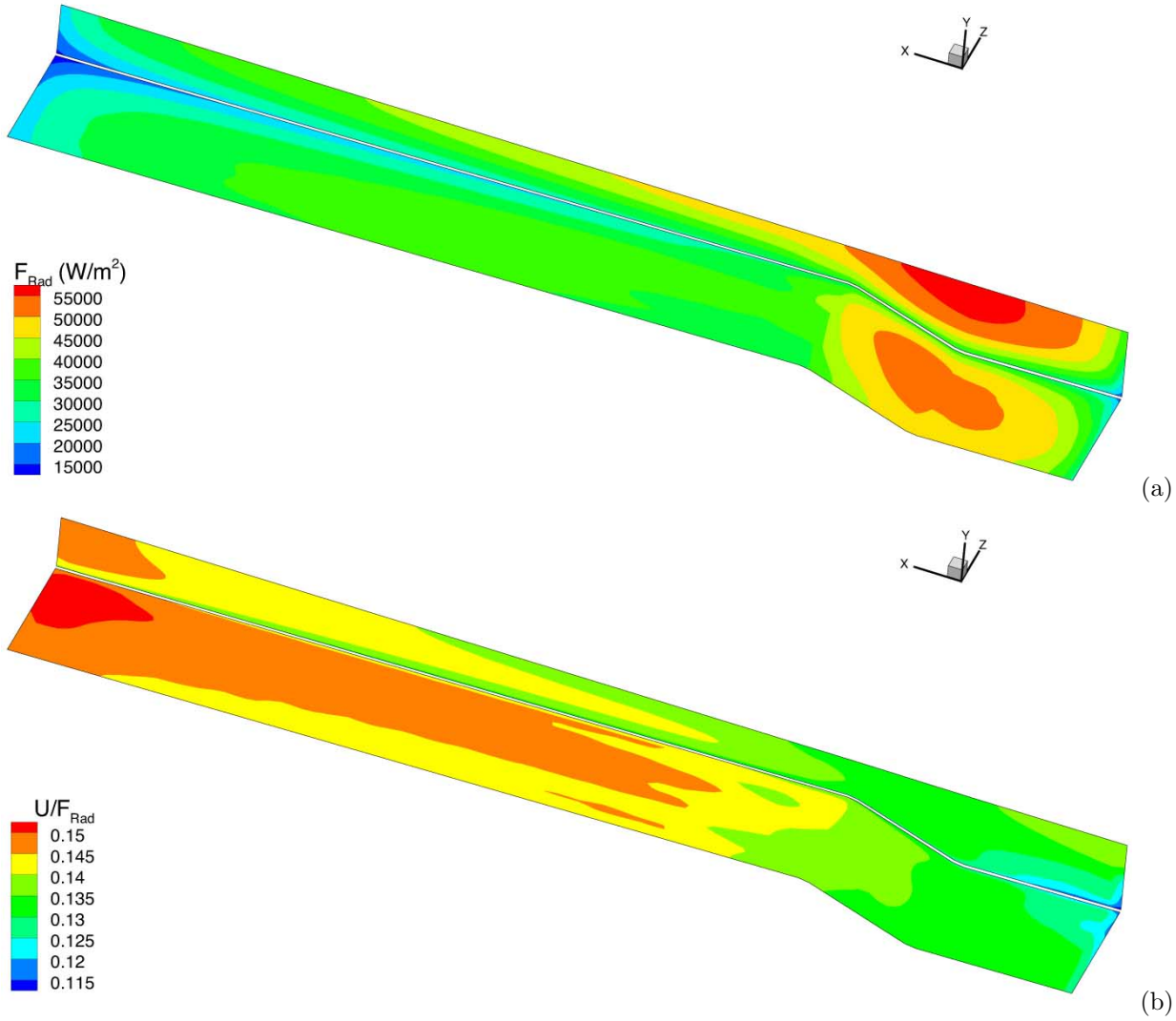

Figure 8. Radiative wall heating (a), and associated total uncertainty (b) from the DOM simulation. Emissivity, reflectivity, and absorptivity equal 0.0, 0.0, and 1.0, respectively.

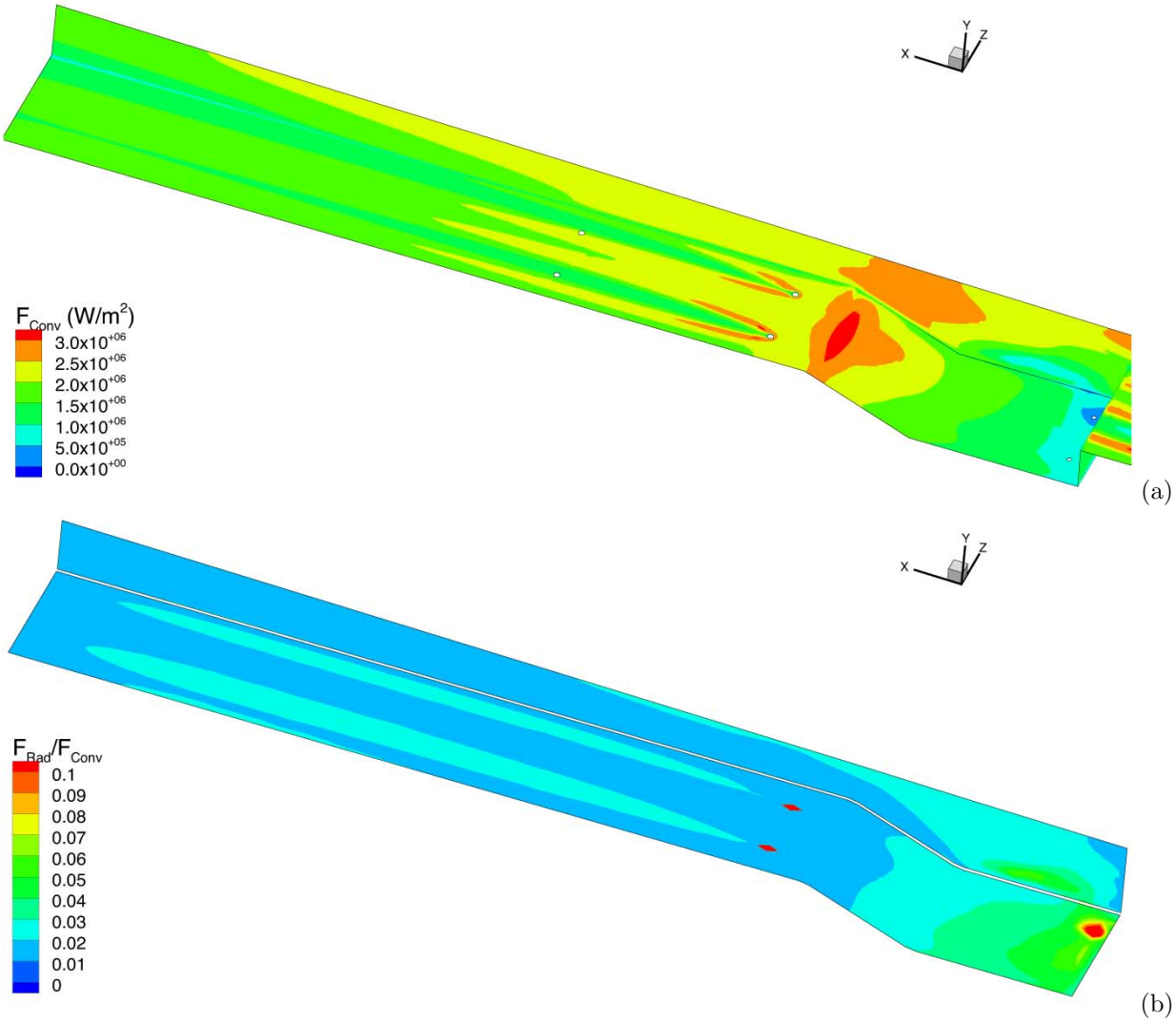

Figure 9. Convective wall heating (a), and relative radiative to convective wall heating (b) from the CFD and DOM simulations

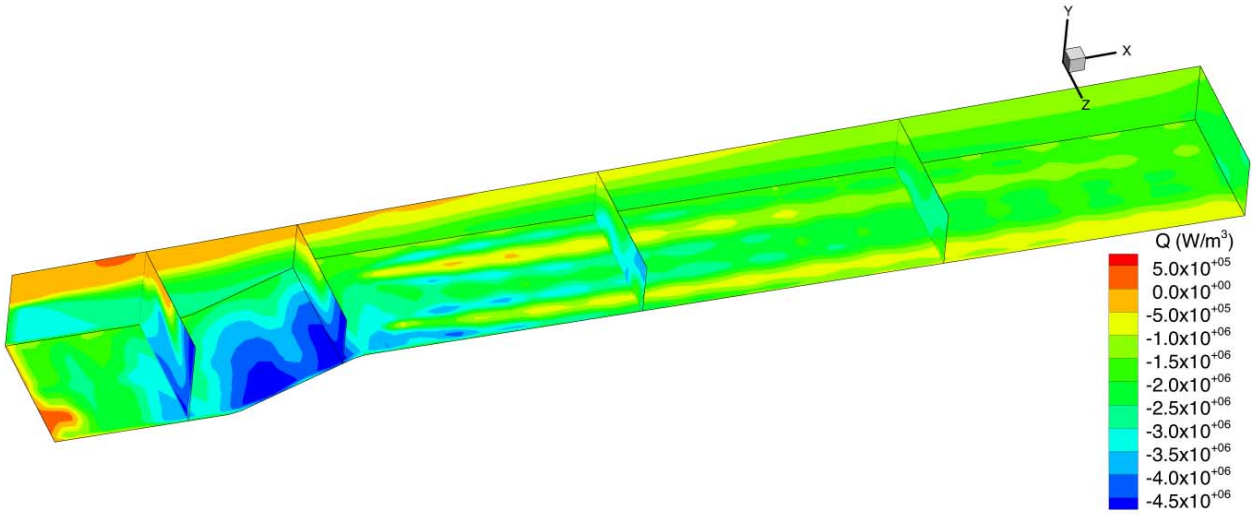

Figure 10. Volumetric radiative heating and cooling in the combustion chamber and flame holder from the DOM simulation

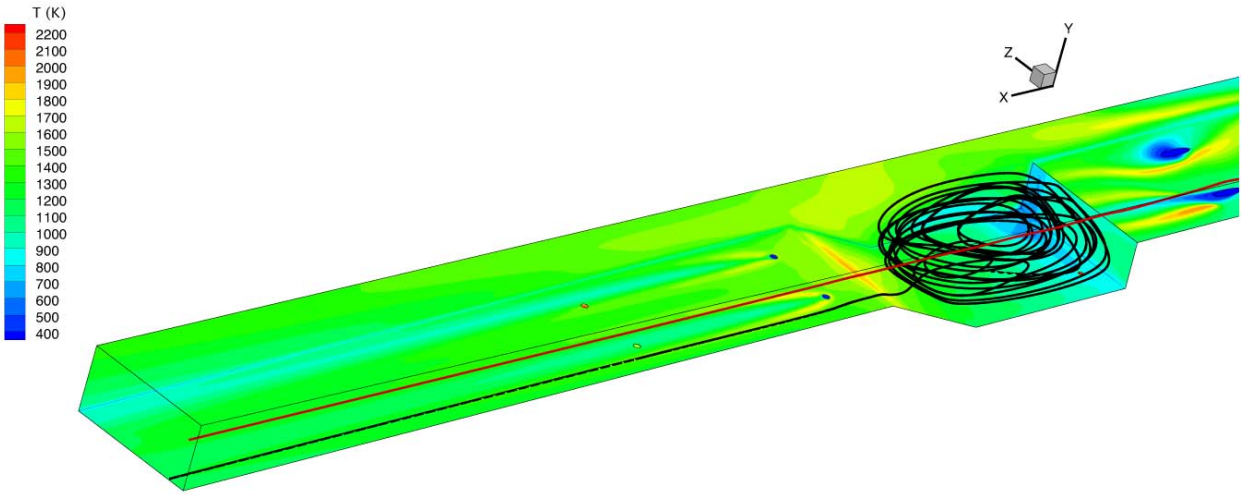

Figure 11. Example stream traces in the HIFiRE-2 test case

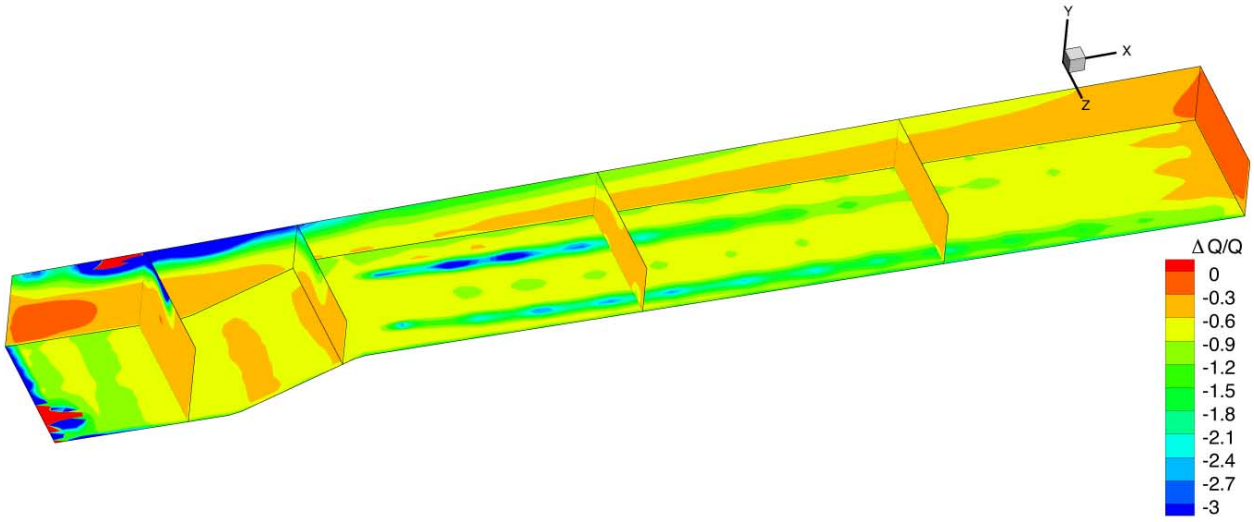

Figure 12. Relative change in volumetric cooling from completely absorbing walls to half-absorbing-half-reflecting walls.

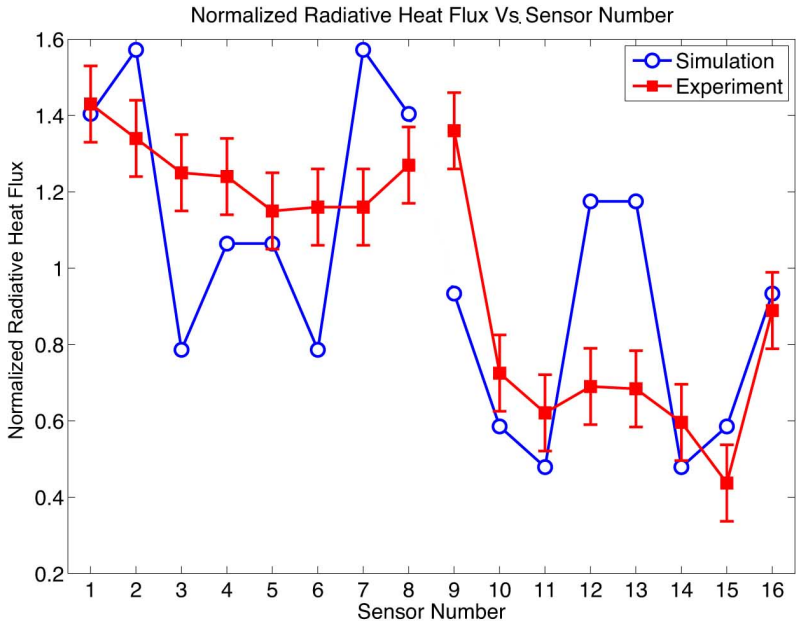

(a)

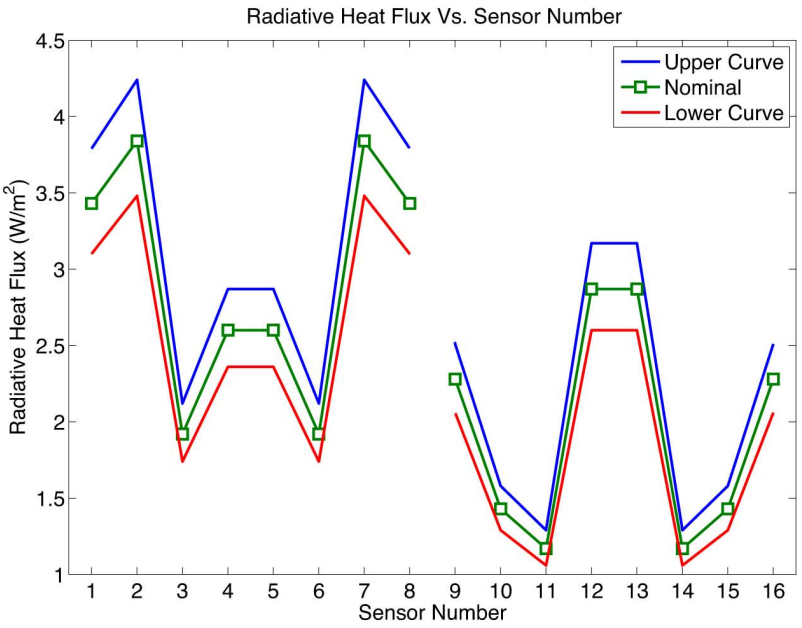

(b)

Figure 13. Simulation and experimental radiative heat flux measurements at exhaust port for normalized experimental data with 10 % error bars (a). Absolute simulation data with variations due to spectral model uncertainty (b).

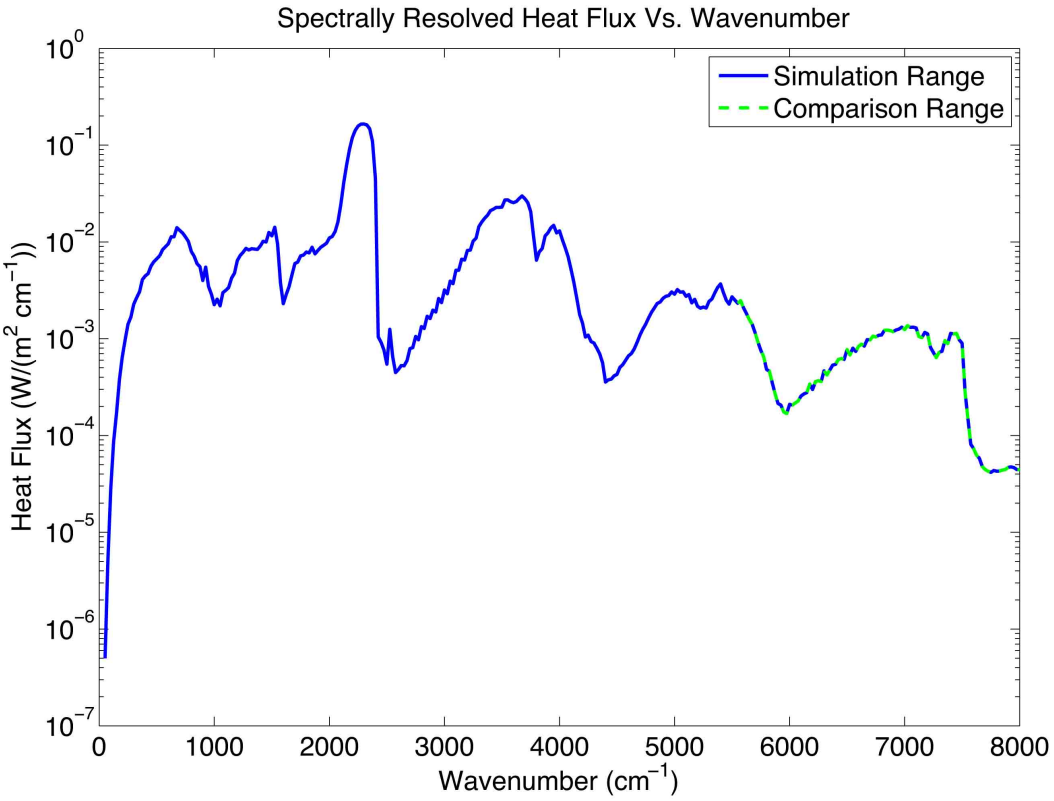

Figure 14. Spectrally resolved radiative heat flux to sensor 1, covering the full simulation range with the spectral range used to compare to the experimental measurements highlighted (5550 to 8000 cm^{-1}).